Water Research 304 (2026) 126362

Contents lists available at ScienceDirect

Water Research

journal homepage: www.elsevier.com/locate/watres

Real-time quantification of nanoplastics deposition in nanofiltration using laser-induced breakdown detection (LIBD)

Tyler A. Malkoske [a], Minh N. Nguyen [a], Susanne Erpel [b], Marcus Wyss [b], Andrea I. Schäfer [a,*]

[a] Institute for Advanced Membrane Technology (IAMT), Karlsruhe Institute of Technology (KIT), Hermann-von-Helmholtz-Platz 1, Eggenstein-Leopoldshafen, 76344, Germany

[b] Swiss Nanoscience Institute, University of Basel, Klingelbergstrasse 82, Basel, 4056, Switzerland

HIGHLIGHTS

- LIBD can quantify the deposition and release of nanoparticles (μg/L) in nanofiltration.
- Distinct particle release mechanisms were observed depending on deposit thickness.
- Increasing permeate flux (above critical flux) in principle enhanced particle deposition.
- Increases in backwash drag force were insufficient to enhance particle release.
- Properties of weathered particles with transport behaviour require further correlation.

GRAPHICAL ABSTRACT

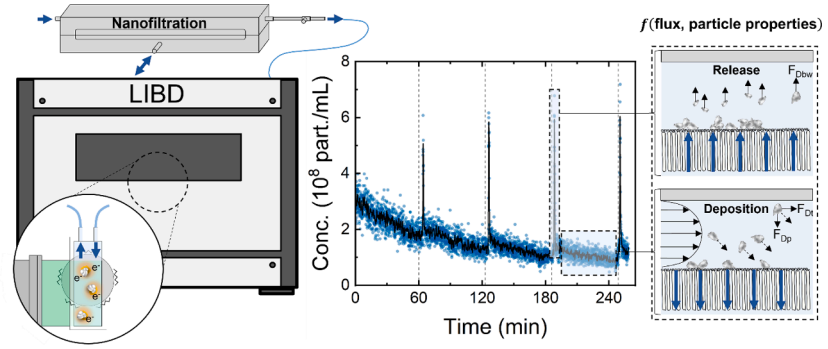

ARTICLE INFO

Keywords:
Drag force
Backwash
Particle release
Adhesion
Electrostatic forces
Particle–membrane interactions
Water treatment

ABSTRACT

Nanofiltration (NF) is an effective barrier for removing nanoplastics (NPs) from water. However, NPs can deposit on the membrane surface and remain even after backwash, altering surface properties and reducing filtration performance. In this study, laser-induced breakdown detection (LIBD) is coupled in-line with a bench-scale NF system to quantify the deposition and release of polystyrene (PS) particles and weathered NPs at environmentally relevant concentrations (1–500 μg/L; 10^7–10^9 particles/mL). Particle deposition during filtration and release during backwash were successfully determined in all experiments, supported by theoretical analysis of the interplay between hydrodynamic and intermolecular forces. At permeate fluxes higher than 100 L/m^2.h, 50–100% of PS particles were deposited by the end of filtration experiments, forming cake layers up to 9 particle diameters thick. In contrast, weak permeate drag forces corresponding to fluxes below 50 L/m^2.h (*i.e.,* just beyond the critical flux) resulted in insignificant deposition. Backwash fluxes from 15 to 57 L/m^2.h exhibited negligible differences in the release of deposited particles owing to only a little increase in backwash drag force. Two mechanisms were observed for the release of NPs during backwash: i) complete release in small circular areas (diameter ≤2 μm) for thin deposits and ii) fracturing of the cake layer for thick deposits. For weathered NPs, irreversible deposition on the membrane surface was observed, although potential particle aggregation and polydispersity must be accounted for to obtain truly quantitative results. The successful quantification of particle

* Corresponding author.
E-mail address: andrea.iris.schaefer@kit.edu (A.I. Schäfer).

https://doi.org/10.1016/j.watres.2026.126362
Received 1 April 2026; Received in revised form 22 June 2026; Accepted 24 June 2026
Available online 25 June 2026

deposition and release showcases LIBD as an effective method for fundamental investigations on NP transport during membrane filtration.

1. Literature

Global plastic production reached approximately 430 million tons in 2019 and is expected to exceed 1,000 million tons by 2060 (OECD). The combination of massive production and unregulated disposal has resulted in plastic pollution becoming a major environmental challenge of global concern (Syberg et al., 2021). Land-based plastic pollution (*e.g.,* mismanaged waste from urban centers (Jambeck et al., 2015, Zhu et al., 2024), industrial and agricultural activities (Zhu et al., 2024, Birch et al., 2020)) is transported to freshwater bodies via contaminated stormwater runoff (Zhang et al., 2023), flooding (Boucher et al., 2019), wastewater effluent (Mason et al., 2016), and landfill leachate (He et al., 2019). Airborne plastic particles can be transported over long distances (>100 km) before deposition during precipitation events (Kernchen et al., 2022), while rivers have been identified as the main pathway by which land-based pollution is transported to oceans (Lebreton and Andrady, 2019). Nanoplastics (NPs; <1 μm) primarily originate from the degradation of larger plastic materials and debris, including microplastics (≥1 μm to <1 mm) (Gigault et al., 2018, Hartmann et al., 2019). NPs are ubiquitous in the aquatic environment (Gigault et al., 2021), where measured concentrations in surface water, groundwater, and oceans range from 0.3−1,500 μg/L (Shi et al., 2024, Xu et al., 2022, Materić et al., 2022, ten Hietbrink et al., 2025). Assuming NPs are represented by a 100 nm diameter sphere with a plastic density of 1 g/cm^3, these measured concentrations are equivalent to 10^6–10^9 particles/mL. Once present in the aquatic environment, NPs can enter the food web and adversely affect the health of organisms, including humans.

NPs enter the food web via uptake and ingestion by plankton, bivalves, and fish (Liu et al., 2024). At environmentally relevant concentrations (0.3−220 μg/L), NPs can disrupt the metabolism, reproduction, and growth of organisms (Besseling et al., 2014, Li et al., 2023, Zhou et al., 2023), altering food webs (Ekvall et al., 2024). Contaminated water is a known human exposure pathway to NPs (Zuri et al., 2023). While NPs have been detected in human tissues, bodily fluids, and organs, further studies are needed to fully understand the consequences of exposure to human health (Ali et al., 2024, Winiarska et al., 2024). While NPs are not currently regulated in drinking water, several states in the U.S. require monitoring of microplastics in source water and drinking water (California Code of Regulations 2018, Feng et al., 2025). Improved analytical capabilities, and solid evidence of negative health impacts are required to develop adequate regulation. To reduce human exposure through contaminated water, drinking water treatment processes are employed for the removal of NPs.

Conventional coagulation−flocculation−sedimentation has been reported to achieve 35−70% removal of NPs of various sizes (10−1,000 nm) and polymer types, while 45% removal can be achieved during sand filtration (Xu et al., 2024). Microfiltration (MF, 0.1−1 μm pore size) and ultrafiltration (UF, 0.01−0.1 μm pore size) membranes remove NPs with diameters >100 nm and >10 nm, respectively. With sub- to single nm pore sizes (Bowen and Mohammad, 1998), nanofiltration (NF) membranes will effectively remove all sizes of NPs. The application of prefilters (5 μm) (Farhat et al., 2020), MF (Van der Bruggen et al., 2005), or UF (Lee and Lee, 2006) prior to NF would substantially reduce the concentration of microplastics and NPs in NF feed water. However, retained NPs may deposit and adhere onto membranes, potentially

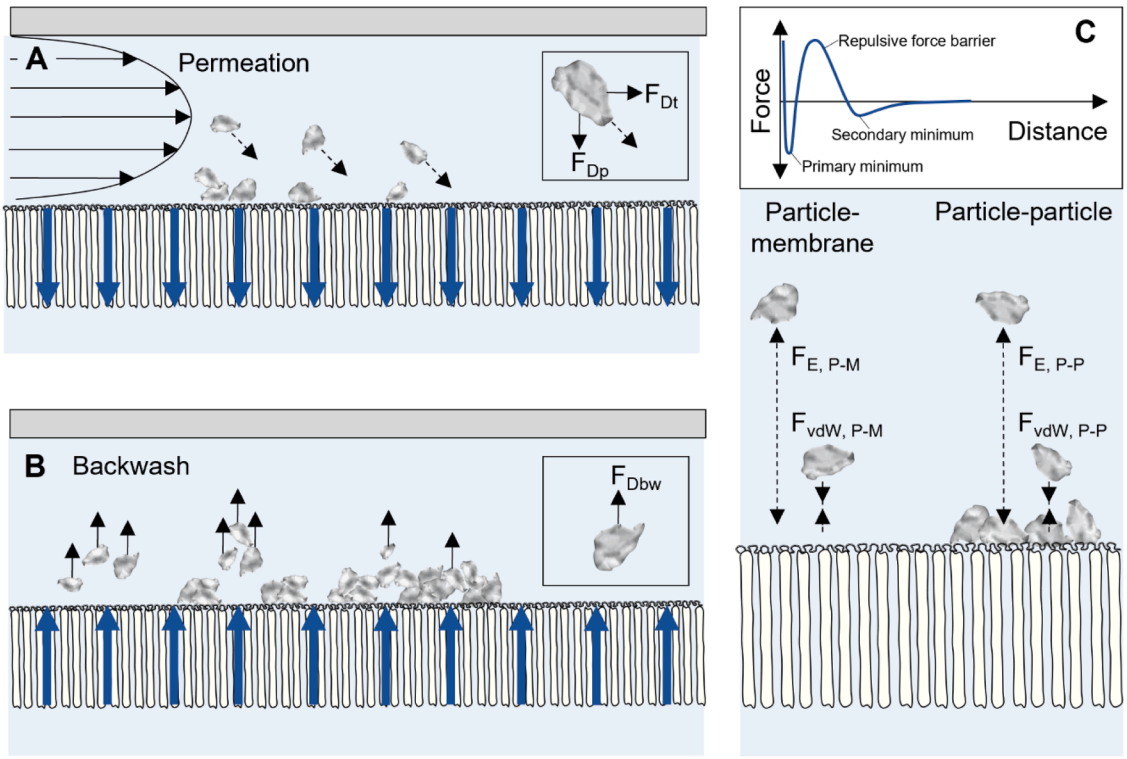

Fig. 1. Hydrodynamic forces exerted on NPs during (A) permeation, (B) backwash, and (C) intermolecular particle-membrane forces between NPs and the membrane, as well as particle-particle forces between NPs in feed water and those deposited on the membrane surface. F_{Dt}, F_{Dp}, and F_{Dbw} are tangential, permeate, and backwash drag forces, $F_{E,\ P-M}$ and $F_{E,\ P-P}$ are particle-membrane and particle-particle electrostatic forces, and $F_{vdW,\ P-M}$ and $F_{vdW,\ P-P}$ are particle-membrane and particle-particle van der Waals forces, respectively.

altering surface properties and performance (*e.g.,* fouling and scaling potential). Elevated concentrations of NPs in membrane retentate require consideration during the selection of tertiary treatment and final waste disposal.

Commercial NF membranes carry a negative surface charge over a wide range of pH values (4−10) (Boussu et al., 2007). While additives and adsorbed material can affect the surface charge of NPs (Blancho et al., 2021), these typically carry a negative surface charge in the environment (El Hadri et al., 2020). As a result, for NPs to deposit onto NF membranes, the interaction energy would need to overcome a potential barrier caused by electrostatic repulsion. Previous studies reported increased organic matter fouling and mineral scaling in the presence of amino-functionalized polystyrene (PS) particles (positive charge) at mg/L concentrations (Yang et al., 2024), as well as increased biofouling with PS particles (Liu et al., 2024, Liu et al., 2025). Due to analytical challenges related to the quantification of NPs at micrograms per liter concentrations, there remains an incomplete understanding of NPs transport during NF and the fundamental link to hydrodynamic and intermolecular forces.

Particle transport in crossflow membrane filtration is the result of hydrodynamic and intermolecular forces (Song and Elimelech, 1995). Hydrodynamic forces consist of permeate drag (F_{Dp}) towards the membrane surface, tangential drag (F_{Dt}) parallel to the membrane surface along the membrane channel (Fig. 1A), and backwash drag (F_{Dbw}) away from the membrane surface during cleaning (Fig. 1B) (Altmann and Ripperger, 1997). Membranes have a heterogeneous surface roughness (*e.g.,* 0.9−130 nm (Fane et al., 2011, Boussu et al., 2007)) that alters hydrodynamic forces at the water–membrane interface, imparting a slip boundary (Lee et al., 2014) and localized water convection (Vrijenhoek et al., 2001). However, membranes are often assumed to be smooth for modelling purposes. When considering submicron particles under laminar flow conditions, back transport due to inertial lift and shear-enhanced diffusion is usually compensated by convection towards the membrane surface (Hong et al., 1997, Cohen and Probstein, 1986, Kim et al., 2006). Gravitational force is considered negligible due to the small size of NPs.

Intermolecular forces consist of particle−particle (F_{P-P}) and particle−membrane (F_{P-M}) forces, evaluated using Derjaguin-Landau-Verwey-Overbeck (DLVO) theory (Derjaguin and Landau, 1941, Verwey, 1947). These forces include electrostatic double-layer interactions (significant at 5−10 nm separation) and van der Waals attraction (significant at < 5 nm) (Fig. 1C) (Israelachvili, 1978, Brant and Childress, 2002). Ultimately, the hydrodynamic and intermolecular forces exerted during membrane operation dictate the extent of particle deposition and adhesion onto the membrane surface.

At the macro-scale, particle deposition during crossflow membrane filtration occurs when hydrodynamic forces (resultant of F_{Dp} and F_{Dt}; Fig. 1A) transport particles to the membrane surface. Upon contact with the membrane surface, the probability of particle adhesion (sticking) is dictated by the magnitude of the repulsive force barrier and hydraulic drag forces (Tang et al., 2011, Liu et al., 2018). When the drag force exceeds the repulsive force barrier, strong particle adhesion occurs within the primary minimum (Fig. 1C). Otherwise, weak adhesion may occur within the secondary minimum at a longer particle−membrane separation distance. Surface roughness increases the effective separation distance between two surfaces, thereby reducing the magnitude of the electrostatic repulsion, and for this reason it is a frequently cited 'scapegoat' for discrepancies between DLVO predictions and experimental observations (Huang et al., 2010). An important practical parameter is the critical flux, which is defined as the threshold flux beyond which convection (*i.e.,* drag forces) overcomes the particle-membrane repulsive force barrier and particle back diffusion, resulting in particle deposition on the membrane (Field et al., 1995, Bacchin et al., 2006). Critical flux depends on hydrodynamics, particle and membrane properties, as well as solution chemistry (Bacchin et al., 2006, Bacchin et al., 1995).

In addition to hydrodynamic forces, cake layer formation plays a key role in particle deposition. During NF, once particle monolayers completely cover the membrane surface, additional deposition results in the development of a cake layer multiple particle diameters thick. Following cake layer formation, particle deposition transitions from being governed by particle-membrane to particle-particle interactions (Liu et al., 2020), and particle interactions within the cake layer can lead to the formation of particle clusters (Lohaus et al., 2020). To limit cake layer formation and flux decline, membrane cleaning is employed to release deposited particles from the membrane surface.

The most common physical cleaning method in NF is crossflow flushing applied in either forward or reverse directions (Al-Amoudi and Lovitt, 2007), which exerts shear stress to lift up the loosely attached particles, and tangential drag forces (F_{Dt}; Fig. 1A) to carry them away. Spontaneous osmotic backwashing (OB) is an alternative cleaning approach, whereby stoppage of the feed pump causes the applied pressure on the feed side of the membrane to drop below the osmotic pressure, resulting in the backflow of water from the permeate side to the feed side of the membrane (Richards et al., 2015). This fluid motion exerts a perpendicular backwash drag force away from the membrane surface (F_{Dbw}; Fig. 1B) and has been applied for NF scaling (Cai et al., 2021) and organic matter fouling (Lee et al., 2021) control. Controlled OB, which includes the application of additional backpressure provided by a pump installed on the permeate side of the membrane, has been investigated for enhancing OB cleaning efficiency. It was reported that up to 2 bars of backpressure can be applied to NF270 membranes over multiple cycles without loss of membrane integrity (*i.e.,* delamination of the active layer) (Cai et al., 2024).

For deposited particles to be released, hydraulic drag forces must overcome particle–membrane and particle–particle interaction forces (Lohaus et al., 2020, Kalde et al., 2023). Incomplete release observed during crossflow flushing suggests that it can be challenging to detach deposited microplastics and NPs (Enfrin et al., 2021, Malkoske et al., 2025). Following cake layer formation, backwash mechanisms include the release of weakly bound particles, cluster breakage, and unfolding of particle bridges (*i.e.,* reorientation to a position of low drag force), as well as cluster fragmentation and resuspension (Lohaus et al., 2020). Once clusters are released, their fragmentation and resuspension occur when hydrodynamic drag forces overcome interparticle attractive forces (Kuznetsova et al., 2007). To account for the complex dynamics of NPs during filtration with NF membranes, the concentration of NPs needs to be monitored in-line at environmentally relevant concentrations, which requires sensitive *in operando* analytical methods.

The quantification of NPs in solution can be achieved using thermally-driven mass spectrometry methods (Santos et al., 2025). These include pyrolysis gas chromatography-mass spectrometry (Py/GC-MS) (Xu et al., 2022) and thermal-desorption proton-transfer--reaction mass spectroscopy (TD-PTR-MS) (Materić et al., 2022, ten Hietbrink et al., 2025) with mass concentration detection limits in the nanograms-per-liter range. Inline quantification of the concentration of NPs can be obtained in pure water matrices at low size and concentration limits of detection (LOD) using light scattering techniques. Single particle counting (SPC) is limited in terms of size LOD (100 nm) (Rossé and Loizeau, 2003). Multi-angle light scattering (MALS) and nanoparticle tracking analysis (NTA) have concentration LODs (10^7–10^9 particles/mL for ≥50 nm particles) (Austin et al., 2020, Filipe et al., 2010) higher than the low end of the environmentally relevant concentration range (10^6 particles/mL).

Laser-induced breakdown detection (LIBD) with acoustic detection provides inline quantification of nanoparticles by detecting plasma shockwaves generated when a focused laser beam triggers the simultaneous release of electrons in large quantities from the nanoparticle surface (Scherbaum et al., 1996, Nguyen et al., 2025). With relatively fast screening (one measurement per 20 seconds), Nguyen *et al.* reported low particle concentration LOD ($2{\cdot}10^6$ particles/mL for 100 nm PS particles and 10^4–10^5 particles/mL for weathered NPs) (Nguyen et al.,

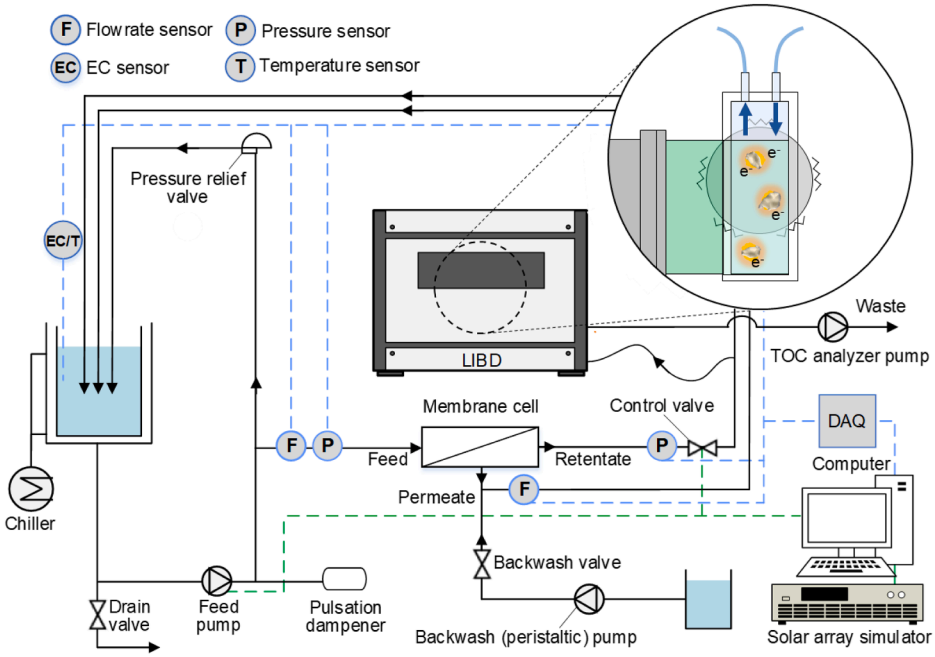

Fig. 2. Bench-scale crossflow filtration system coupled with LIBD.

2025).

In this study, a bench-scale crossflow filtration system was coupled with LIBD to address the following main research questions; i) can LIBD be used for the real-time quantification of NPs deposition and release during NF?, ii) what is the relationship between operating conditions (permeate and backwash flux) and the deposition and release of NPs?, and iii) how do the deposition and release of NPs change as a function of NP properties (concentration, diameter, standard PS particles vs. weathered NPs)? The results obtained provide critical insights into the potential application of LIBD for investigating the fate of NPs during NF and elucidating the deposition and release behavior of NPs under variable operating conditions.

2. Materials and methods

2.1. Bench-scale crossflow filtration system and experimental protocol

Filtration experiments were conducted using a bench-scale crossflow filtration system (described previously (Cai et al., 2022)) coupled with LIBD (Fig. 2). Both HydraCoRe10 (HY10, Nitto Hydranautics, USA) and NF270 (DuPont FilmTec, USA) membranes (active area = $4.7{\cdot}10^{-3}$ m^2) were selected to investigate the effect of pore size and membrane material on the deposition and release of NPs. The properties of HY10 and NF270 membranes are provided in Table S1. During filtration experiments, a portion of the membrane retentate was continuously drawn through the LIBD via a t-connection installed downstream of a diaphragm valve using a TOC analyzer (Sievers M9, Veolia Water Technologies & Solutions, France) at a flow rate of 1 mL/min. Backwash flux was provided by a peristaltic pump installed on the permeate side of the membrane cell. During all filtration experiments a chiller (Lauda-Brinkmann, MC250, Germany) was used to maintain a feed water temperature of 24 ± 2°C.

Filtration experiments consisted of four cycles of 60 min filtration followed by a 3 min backwash, and finally a shortened filtration period of 15 min to enable quantification of backwash efficiency following cycle #4. At the start of each filtration experiment, 100 mL of permeate was diverted to a beaker for use as backwash water. Backwash flux was constrained by maximum pump speed (equivalent to a backwash flux of 60 L/m^2.h) and maintaining membrane integrity (*i.e.,* avoiding delamination) (Cai et al., 2024). Following backwash, the feed pump was operated at a low speed for the first 5 min of permeation to decrease the flow rate in the retentate line and capture a greater volume of the backwash for quantification of NPs using LIBD. A summary of conditions applied during filtration experiments is provided in Table S2, and the filtration protocol is provided in Table S3.

Variability in feed, permeate, and backwash flow rates due to pump pulsation contributed to errors in calculated hydrodynamic drag forces. The fluctuation of feed and permeate flow rates was <10% (diaphragm pump), while that of backwash flow rate was 30% (peristaltic pump). To verify that particle aggregation did not contribute to erroneous LIBD measurements, an additional filtration experiment was conducted under conditions selected to maximize particle deposition and release, and grab samples were analyzed with NTA for particle size and concentration. These conditions included the use of an HY10 membrane, a high concentration of 100 nm PS particles (~$9{\cdot}10^8$ particles/mL; near the upper limit of NTA), high backwash flux (~57 L/m^2.h), and maximum system pressure (19 bar).

2.2. Feed water preparation and sample analysis

Feed water consisted of 5 L Milli-Q water with 10−500 μg/L PS particles, or 1 μg/L weathered NPs. Background electrolytes consisted of 1 mM $NaHCO_3$ (EMSURE grade powder, Merck Millipore, USA) and 10 mM NaCl (99.5% powder, Thermo Scientific, USA), resulting in an osmotic pressure of 0.5 bar. Feed water pH was approximately constant at 8.2 ± 0.1, verified with the SenTix 81 probe attached to the pH/cond 3320 Multimeter (WTW, Germany). Feed water and permeate grab samples were collected during each of cycles #1 to #4. During cycle #1, feed water samples were collected at 0, 10, 30, and 60 min, and a single permeate sample was collected at 60 min. Subsequently, feed water and permeate samples were collected at the end of cycles #2 (120 min), #3 (180 min), and #4 (240 min). The volume of each grab sample (25 ± 0.5 mL) was confirmed gravimetrically to account for system losses in mass-balance calculations. To enable the quantification of membrane salt retention, feed water conductivity was measured using an inline electrical conductivity (EC) sensor and permeate grab samples were analyzed using a portable EC probe (TeraCon 325 probe, WTW).

2.3. Nanoplastics preparation and characterization

Filtration experiments were performed using both PS particles (Applied Microspheres, Netherlands) with a range of sizes (50, 85, 100, 150, 200, 400 nm) and concentrations (10, 30, 100, 200, 300, 400, 500 μg/L), and weathered PS nanoplastic fragments (weathered NPs) prepared at Tel Aviv University in Israel. To prepare weathered NPs, bulk plastic materials were crushed and then exposed to accelerated oxidative, mechanical, and thermal degradation to simulate environmental weathering processes (Sarkar et al., 2021). In previous work, weathered NPs were characterized in terms of size (~110 nm) and concentration using NTA (NanoSight NS3000, Malvern Panalytical, UK) and the colloidal stability of PS particles and weathered NPs was confirmed over 7 hrs using DLS (Litesizer 500, Anton Paar, Switzerland) (Nguyen et al., 2025). Weathered NPs exhibited a larger size distribution and polydispersity when compared to PS particles. The zeta potential of PS particles was determined as a function of pH by performing triplicate measurements using electrophoretic light scattering (also Litesizer 500). Samples were prepared in Milli-Q water with background electrolytes to ensure uniform solution conductivity (1.2 ± 0.3 mS/cm) over all electrophoretic mobility measurements. As the electrophoretic readings were not reliable at low particle concentrations (Fig. S1), the zeta potential values used in subsequent calculations were based on measurements attained at a particle mass concentration of 10 mg/L. Zeta potential values for 50, 85, 100, 150, 200, and 400 nm particles were −39 ± 4, −33 ± 4, −20 ± 4, −26 ± 4, −25 ± 4, −29 ± 4 mV, respectively (Fig. S1).

In LIBD, particle aggregation could present a challenge if the clusters detached from the membrane surface do not fragment and resuspend before measurement. Aggregation can cause variability in LIBD as larger clusters could mask the signal produced by smaller NPs (Walther et al., 2004). Offline NTA (violet laser, 405 nm wavelength, NanoSight Pro, Malvern Panalytical, UK) was employed to verify that the aggregation of PS particles (100 nm) in membrane retentate did not occur during filtration experiments. Grab samples of the feed water (0 min) and retentate, collected just before and after each backwash, were each analyzed five times. Both the average size and particle concentration obtained from the size distribution data are reported in Fig. S2 and Fig. S3, respectively. As results showed that there were no significant changes in particle size during filtration and backwash, PS particle aggregation was considered negligible under the conditions applied during filtration experiments. Aggregation of weathered NPs was not examined because the applied feed concentration (1 μg/L, or ~10^6 particles/mL) was below the detection limit of NTA (10^7 particles/mL).

2.4. Laser-induced breakdown detection (LIBD) for nanoplastics quantification

The LIBD system consisted of a pulsed neodymium-doped yttrium aluminum garnet (Nd:YAG) laser (Flare NX 515-0.6-2, Coherent, France) operated at a wavelength of 515 nm. During operation, the laser beam was directed into a flow-through cuvette (optical path length 1 cm, volume 0.75 mL, product ID 175.000-QS, Hellma Analytics, Germany), which induced dielectric 'breakdowns' of particles that were detected acoustically by a piezo crystal (custom-made, Dittel, Germany). The laser pulse energy was fixed at 240 μJ, which is close to the maximum laser energy (245−250 μJ). The number of pulses per measurement was 600, and the measurement rate was 150 Hz (4 s per data point) to allow for the inline detection of spikes in particle concentration during backwash. For 100 nm PS particles, the LOD for LIBD was $2{\cdot}10^6$ particles/mL (0.5 μg/L) and the upper threshold of detection was $2{\cdot}10^9$ particles/mL (1,000 μg/L). Both the LOD and upper threshold of detection varied with the size of PS particles (Nguyen et al., 2025). The relative error of breakdown probability (BDP) for particle deposition observed during filtration experiments was 15−20%, similar to that previously reported for the same LIBD system (Nguyen et al., 2025). The absolute error of BDP for particle release was determined based on the linear regression of standard deviation values from a calibration performed using 100 nm PS particles (Fig. S4).

2.5. Visualization of nanoplastic deposits

Following filtration experiments, membrane samples were removed from the membrane cell of the bench-scale crossflow filtration system and cut into four quarters. The third and fourth quarters from the channel inlet were freeze-dried (Alpha 2-4 LSC plus, Germany) for 22 hrs at −20 °C and 0.0001 mbar (Imbrogno et al., 2025) then delivered to the Nano Imaging Lab of the Swiss Nanoscience Institute (SNI) at the University of Basel for imaging using scanning electron microscopy (SEM; GeminiSEM 450 equipped with an Everhart−Thornley secondary electron detector, Zeiss, Germany).

At the Nano Imaging Lab, 5 mm · 10 mm pieces were cut from each membrane sample. These pieces were then bent over their long side, and both ends were held together using a pair of tweezers. In this position, they were immersed in liquid nitrogen for three minutes, then cut with a scalpel. The two resulting halves were mounted onto a small aluminum plate with a carbon sticker, and then the aluminum plate was placed into a SEM holder in the upright position. Finally, the samples were sputter-coated with 20 nm gold using a sputter coater (EM ACE600, Leica, Germany) to allow good imaging contrast while being able to resolve PS particles and weathered NPs. Imaging of the membrane surface and cross-section was performed at a fixed acceleration voltage of 3 keV and magnifications between 500 and 40,000 (approximately 1.0 nm resolution). The thickness of PS particle deposit layers was determined several times at three different positions on each of the membrane samples.

2.6. Particle deposition and release calculations

Breakdown probability (BDP) was calculated from LIBD measurements using an Excel 2016 macro (TZW, Germany), then converted to particle concentration (particles/mL) using calibration curves for PS particles and weathered NPs provided in a previous study (Nguyen et al., 2025). Particle concentration data were smoothed by performing locally-weighted regression using the locally estimated scatterplot smoothing (LOESS) method in Origin Pro 2021b software (OriginLab, USA) (Cleveland, 1979). The fitted curve was within the analytical error of LIBD and provided a continuous representation of data to enable peak integration in Origin Pro.

The number of particles irreversibly deposited on the membrane surface following each cycle was calculated using a mass-balance approach:

$$c_{end}V_{end} - c_0V_0 + \left(c_{LIBD}V_{LIBD} + c_{sample}V_{sample}\right) \quad (1)$$

where c_{end}, c_0, c_{LIBD}, and c_{sample} are the particle concentrations (particles/mL) in membrane retentate following backwash, at the beginning of each cycle, in the LIBD sample stream, and in retentate grab samples, respectively. V_{end}, V_0, V_{LIBD}, and V_{sample} are the volumes (mL) of feed water following backwash, feed water at the beginning of each cycle, the LIBD sample stream following each cycle, and retentate grab samples, respectively. The cumulative number of particles irreversibly deposited over multiple cycles was calculated as the sum of particles deposited following each individual cycle. In completing the mass balance, it was assumed that i) PS particles and weathered NPs were homogeneously distributed in the feed tank, sample stream, and grab samples, ii) particle aggregation and losses within the bench-scale crossflow filtration system were negligible, and iii) the sample flow rate provided by the TOC analyzer pump was indeed constant at 1 mL/min. The volume of water lost from the system during each filtration experiment was approximately 250 mL (V_{LIBD}) from continuous flow through the LIBD and 275 mL from grab samples (V_{sample}), or 525 mL in total. Assuming a homo-

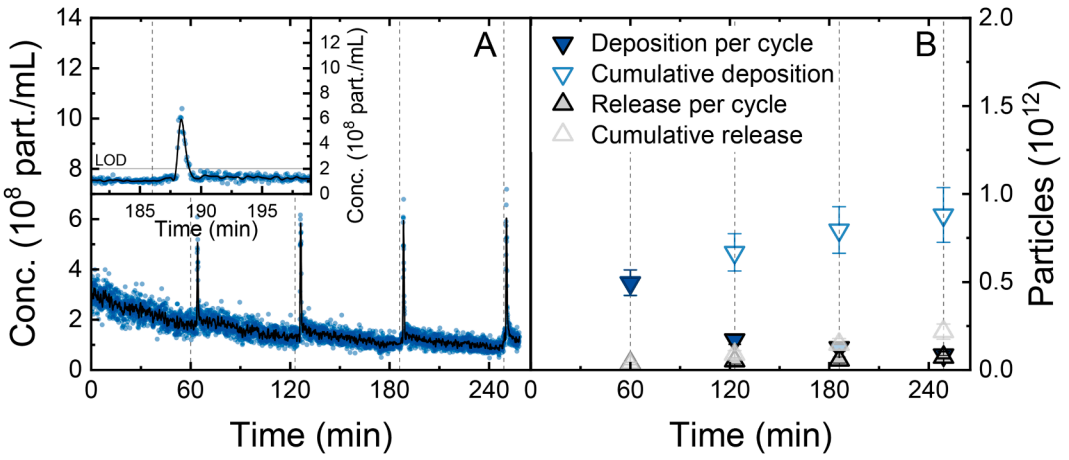

Fig. 3. (A) Retentate concentration of PS particles with a magnified peak from release during backwash following cycle 3 (inset), and (B) deposition and release of PS particles over four cycles. Feed water: 100 μg/L of 100 nm PS particles, 1 mM $NaHCO_3$, 10 mM NaCl; HY10 membrane; 500 L/m^2.h permeate flux, 54 L/m^2.h backwash flux.

geneous distribution of PS particles and weathered NPs, this volume contained approximately 10% of the particles in the system at the start of each filtration experiment.

For particle release, only BDP peaks that exceeded the mean value of the last 40 measurements of a cycle plus three times the standard deviation (*i.e.,* LOD) were considered quantifiable. Particle release during each backwash was quantified by integration to determine the peak area (particles min/mL), and then multiplying the peak area by the average retentate flow rate (mL/min) following backwash. The cumulative number of particles released over multiple cycles was calculated as the sum of particles released following each backwash. The approach utilized to estimate the error for particle release is presented in Fig. S5.

To analyze whether particle deposition could cause permeate flux decline, the cake layer resistance of spherical particles was estimated using the Carman−Kozeny equation (Belfort et al., 1994) (Table S4). For 100 nm diameter spherical particles and the NF270 membrane, assuming a membrane permeability of 17 ± 1 L/m^2.h.bar and feed water temperature of 20 °C, a cake layer approximately 21 particle diameters (~2 μm) thick would be required to create a 1% permeate flux decline. As such, NPs at environmentally relevant concentrations are unlikely to result in substantial permeate flux decline on their own.

2.7. Hydrodynamic and intermolecular force calculations

Hydrodynamic forces were estimated in terms of permeate (F_{Dp}), tangential (F_{Dt}), and backwash (F_{Dbw}) drag forces, and particle-membrane and particle-particle intermolecular forces estimated in terms of electrostatic ($F_{E,\ P-M}$, $F_{E,\ P-P}$) as well as van der Waals (F_{P-M}, F_{P-P}) (*i.e.,* DLVO) forces. Equations and assumptions used to calculate hydrodynamic and intermolecular forces are summarized in Table S5. Particle trajectories within the membrane channel were estimated based on hydrodynamic forces, assuming Poiseuille flow between parallel plates (Hwang et al., 1997) in the x-direction, uniform flow distribution in the y-direction, and no-slip boundary conditions (Fig. S6). Critical flux beyond which particle deposition occurs was estimated using the model provided by Bacchin *et al.* (Bacchin et al., 2006, Bacchin et al., 1995). Equations used to estimate critical flux are provided in Table S6, and estimated values for different particle sizes are presented in Fig. S7.

2.8. Error analysis

The analytical error of the LIBD system (15−20%) represented the main source of uncertainty in the quantification of particle deposition and release. The fitted curve obtained using the LOESS method, which was used to quantify particle release, was within the analytical error of LIBD. In comparison, errors in the volume of water in the system and losses during sampling and collection of grab samples due to volumetric flask tolerance (V_0), TOC pump flow rate (V_{LIBD}), and analytical balance tolerance (V_{sample}) were considered negligible. A summary of error sources for parameters measured during filtration experiments and those calculated based on experimental results is provided in Table S7.

3. Results and discussion

While NF represents an effective barrier for removing NPs from water, the fate of NPs during NF is not fully understood. To elucidate deposition and release behavior, LIBD was coupled with a bench-scale crossflow filtration system, and the concentration of NPs in membrane retentate was measured. Filtration experiments were conducted to determine if LIBD could be used to quantify the deposition and release of PS particles in real-time over consecutive NF cycles. Next, membrane flux values and the properties of PS particles were systematically varied to link changes in hydrodynamic drag forces and intermolecular forces with the observed deposition and release behavior. Finally, the potential application of LIBD to quantify the deposition and release of environmentally relevant weathered NPs was assessed.

3.1. Quantification of particle deposition and release using LIBD

To determine whether LIBD can be used to quantify the deposition and release of NPs in real time during NF, the concentration PS particles in membrane retentate was continuously measured over four consecutive cycles (Fig. 3). It was expected that during permeation, the concentration of PS particles in the retentate would decrease as particles deposited onto the membrane, while the subsequent release of particles during backwash would cause a spike in retentate concentration.

The concentration of PS particles in membrane retentate decreased during permeation, and clear spikes exceeding the LOD ($2{\cdot}10^6$ particles/mL) for LIBD were observed following backwash for each cycle (Fig. 3A). Particle deposition per cycle decreased as the number of PS particles remaining in the feed water declined, while cumulative deposition continued to increase until the end of the filtration experiment (Fig. 3B). Approximately 41% of all PS particles present in the feed water ($1.5 \pm 0.1{\cdot}10^{12}$ particles) deposited after the first cycle, sufficient to entirely cover the membrane surface. Over each subsequent cycle, 33−37% of the PS particles that remained in the feed water deposited, suggesting the formation of a cake layer multiple particle diameters thick. The low release efficiency during backwash (6% of deposited particles) indicates that the applied backwash drag force was insufficient to fully overcome

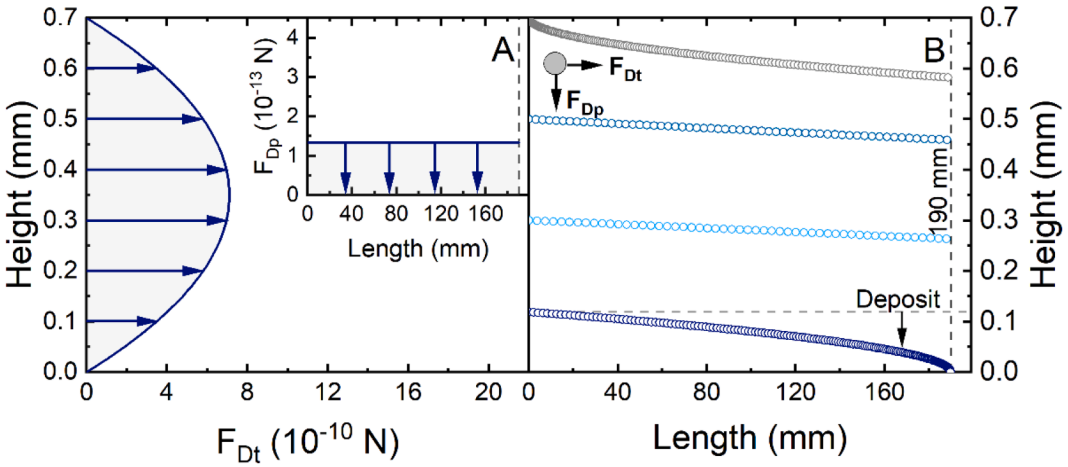

Fig. 4. (A) Calculated tangential and permeate (inset) drag forces exerted over the height and length of the channel, and (B) the estimated trajectories of particles after entering the channel at different heights from the membrane surface (0.70, 0.50, 0.30, and 0.12 mm, the maximum depth for deposition). Calculations are based on 500 L/m^2.h permeate flux, 0.5 L/min feed flow rate, and 100 nm PS particles. Note: x- and y-axes in (B) are not shown to scale.

particle−membrane and particle−particle attractive interactions required for particle release. These results demonstrate that LIBD is effective for quantifying the deposition and release of NPs even at environmentally relevant particle concentrations (10^6 part./mL), which are below the LOD for other state-of-the-art inline methods such as MALS ($\geq 10^8$ part./mL) (Austin et al., 2020) and NTA (10^7–10^9 part./mL) (Filipe et al., 2010, Gross et al., 2016). To determine if there was a theoretical basis to support the observed particle transport, both hydrodynamic and interfacial forces affecting particle deposition were estimated.

The potential for particle deposition was assessed at the macro-scale by considering the hydrodynamic conditions within the channel of the membrane cell. The anticipated particle trajectories based on calculated tangential and permeate drag forces are presented in Fig. 4.

Tangential drag forces (F_{Dt}) in the crossflow direction were three orders of magnitude greater than the permeate drag force (Fig. 4A). As such, at a flux of 500 L/m^2.h the x-component of the resultant force along the channel length was substantially larger than the y-component towards the membrane surface. For deposition to occur, particles needed to enter the channel at a height ($\leq$0.12 mm) near the membrane surface

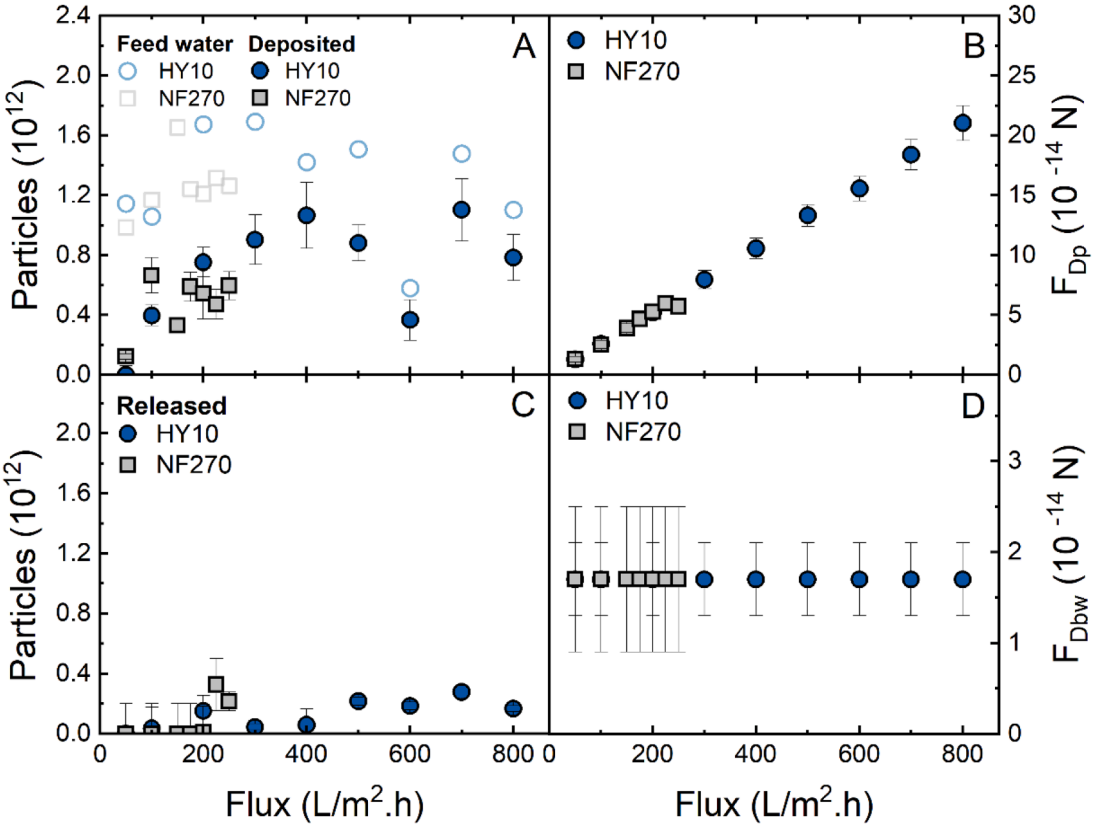

Fig. 5. Cumulative deposition of PS particles and permeate drag forces (A and B), as well as total release of PS particles and backwash drag forces (C and D) during filtration experiments using HY10 and NF270 membranes over a range of permeate flux values (50–800 L/m^2.h). Feed water: 100 μg/L of 100 nm PS particles, 1 mM $NaHCO_3$, 10 mM NaCl; 54 L/m^2.h backwash flux.

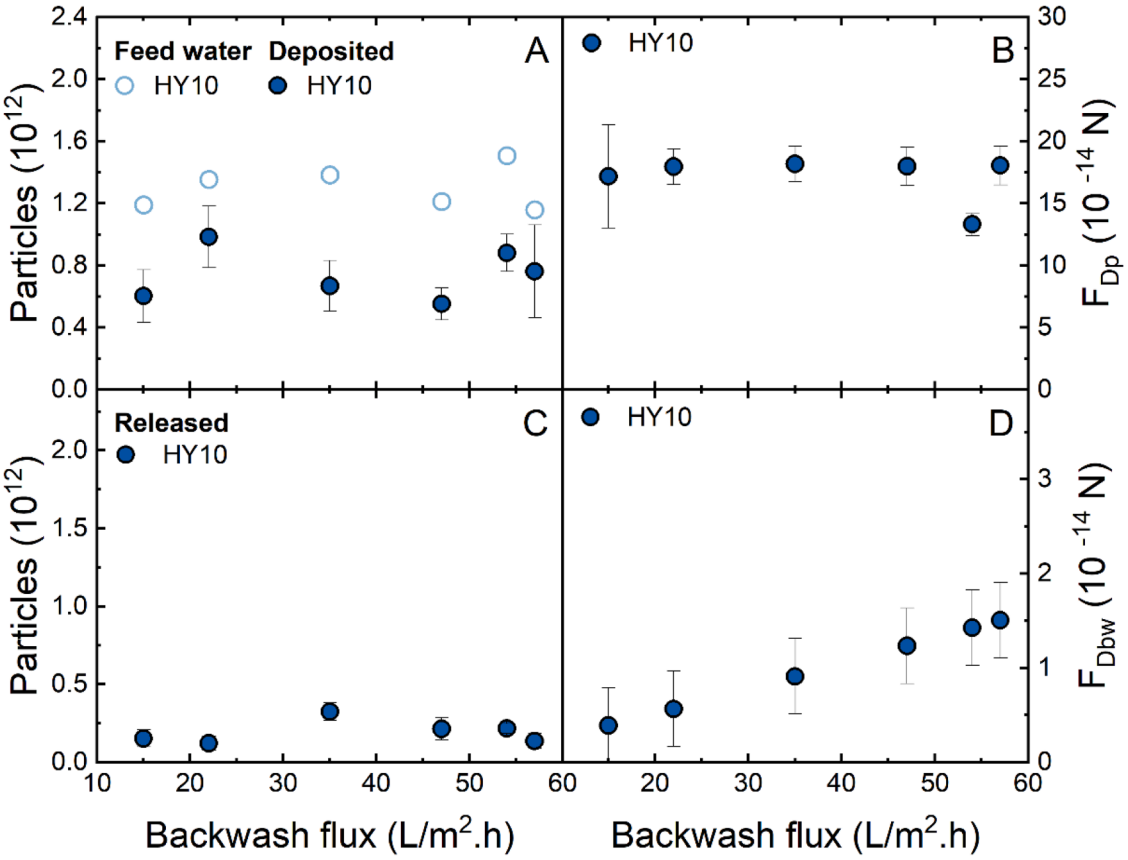

Fig. 6. Cumulative deposition of PS particles and permeate drag forces (A and B), as well as total release of PS particles and backwash drag forces (C and D) during filtration experiments conducted over a range of backwash flux values (15–57 L/m^2.h). Feed water: 100 μg/L of 100 nm PS particles, 1 mM $NaHCO_3$, 10 mM NaCl; HY10 membrane; 500 L/m^2.h permeate flux.

(Fig. 4B) (Hwang et al., 1997). Particles that entered at a height >0.12 mm were not expected to deposit before exiting the channel. Considering the maximum height (≤0.12 mm) at which particles entering the channel could deposit and assuming homogeneous particle mixing throughout the system, it was estimated that 17% of particles in the feed water deposited with each pass of the membrane, or approximately 67% following each permeation cycle. According to the analysis of DLVO forces, particle deposition was anticipated to occur within 15−50 nm distances from the membrane surface/cake layer, where weak particle−membrane and particle−particle attractions occurred via van der Waals forces (Fig. S8). These distances might be overestimated. Huang *et al.* predicted similar particle−membrane separation distances for nanometer-sized particles, assuming a smooth membrane surface, but demonstrated that the incorporation of surface roughness into their model substantially reduced the repulsive force barrier and separation distance (Huang et al., 2010). Additionally, the attraction energy between hydrophilic membranes and hydrophobic particles can be enhanced due to Lewis acid−base electron sharing, which further reduces the particle−membrane separation distance (Brant and Childress, 2002).

Macro-scale analysis of the expected particle trajectories suggested that substantial deposition could occur over the course of a filtration experiment, which is consistent with the particle deposition measured using LIBD. Next, the relationship between particle deposition and the magnitude of permeate drag forces was investigated.

3.2. Particle deposition as a function of permeate drag force

To establish a link between particle deposition and permeate drag force, cumulative particle deposition was quantified following four cycles over a range of permeate flux values (50–800 L/m^2.h) for HY10 and NF270 membranes (Fig. 5). Anticipated particle trajectories are provided in Fig. S9. Feed pressure, feed and permeate conductivities, feed flow rate, as well as permeate and backwash flow rates during filtration experiments using HY10 and NF270 membranes are provided in Fig. S10 and Fig. S11, respectively. The concentration of PS particles measured in membrane retentate using LIBD is provided in Fig. S12 (HY10) and Fig. S13 (NF270).

For HY10 membranes, particle deposition was observed from 100 L/m^2.h (insignificant at 50 L/m^2.h), while for NF270 membranes, deposition occurred from 50 L/m^2.h (Fig. 5A). While increasing permeate drag force (Fig. 5B) was expected to increase particle deposition (Tang et al., 2011), cumulative particle deposition was similar at flux values ≥100 L/m^2.h as the majority (50–100%) of particles present in the feed water at the start of the filtration experiments deposited following four cycles. These flux values exceeded the critical fluxes estimated for HY10 (29 L/m^2.h) and NF270 (32 L/m^2.h) membranes (Fig. S7), which were comparable to those reported (29–35 L/m^2.h) for the filtration of negatively charged organic colloids (Mänttäri and Nyström, 2000). Deposition trajectories (Fig. S9) indicated that as flux increased from 100 to 800 L/m^2.h, the maximum height (distance from the membrane) that particles entering the channel could deposit increased from 0.05 to 0.15 mm. As a result, it was expected that 70–98% of particles in the feed water would deposit following four cycles, which was within the range observed using LIBD. Analysis of DLVO forces suggested that particle deposition occurred at particle−membrane separation distances of 15 nm (Fig. S8), as the repulsive force barrier at shorter separation distances was two to three orders of magnitude greater than the permeate drag force towards the membrane surface.

When considering particle release during backwash, for HY10

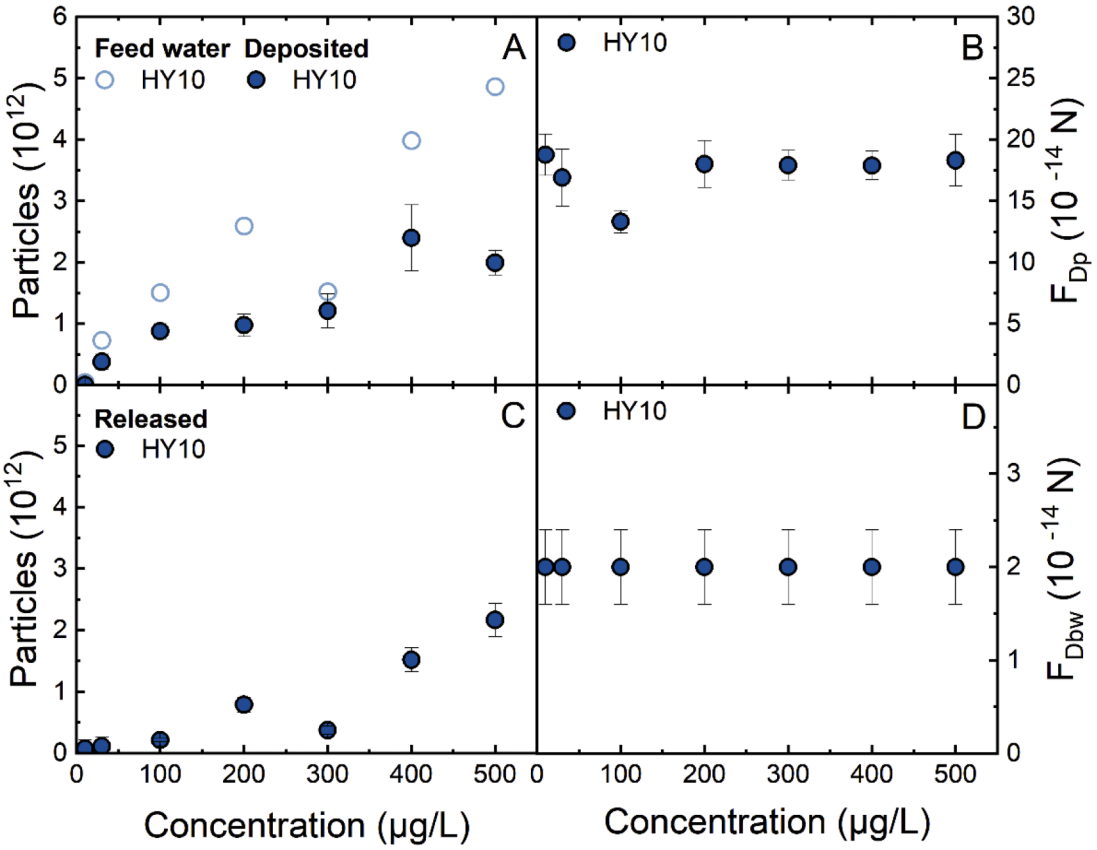

Fig. 7. Cumulative deposition of PS particles and permeate drag forces (A and B), as well as total release of PS particles and backwash drag forces (C–D) during filtration experiments conducted using feed water with a range of PS particle concentrations (10–500 µg/L). Feed water: 100 nm PS particles, 1 mM $NaHCO_3$, 10 mM NaCl; HY10 membrane; 500 L/m^2.h flux, 54 L/m^2.h backwash flux.

membranes, a weak increasing trend was observed with permeate flux, which was partially masked by variations in the initial concentration of PS particles in feed water as well as the number of deposited particles (Fig. 5C). The quantity of released particles varied consistently with the quantity of deposited particles (at a ratio of 0.5), where the backwash drag force remained constant (Fig. 5D). For NF270 membranes, particle release was insignificant except at the highest permeate flux values. Overall, particle deposition was similar at fluxes ≥100 L/m^2.h (exceeding the critical flux), which caused the majority of PS particles to deposit by the end of the filtration experiments. Next, the potential to enhance particle release by increasing backwash drag force was considered.

3.3. Particle release as a function of backwash drag force

To determine if particle release could be enhanced by increasing backwash drag force, filtration experiments were conducted over a range of backwash flux values (15–57 L/m^2.h; Fig. 6). Feed pressure, feed and permeate conductivities, feed flow rate, as well as permeate and backwash flow rates during filtration experiments using HY10 membranes are provided in Fig. S14. Particle concentrations measured in membrane retentate using LIBD are presented in Fig. S15.

Cumulative particle deposition ($0.4-1.2{\cdot}10^{12}$ particles) following four cycles did not vary significantly over filtration experiments (Fig. 6A). As the applied permeate flux values and drag forces were constant (Fig. 6B), the similarity in particle deposition observed for each experiment indicates that increases in backwash flux did not enhance particle release. Quantification of particle release during backwash confirmed similar release efficiency (7−15% of deposited particles) despite increasing backwash flux (Fig. 6C). Analysis of backwash drag forces revealed that although backwash flux increased by nearly four times from the lowest to the highest applied values, only modest increases in backwash drag force were achieved (Fig. 6D).

Particle release did not increase over the applied range of backwash flux values because only modest increases in backwash drag force were achieved. Next, the relationship between particle properties and particle deposition and release behavior was investigated.

3.4. Variation of deposition and release with particle concentration

To elucidate how particle deposition and release change with particle concentration, filtration experiments were performed using feed water with particle concentrations ranging from 10 to 500 µg/L (Fig. 7). Feed pressure, feed and permeate conductivity, feed flow rate, as well as permeate and backwash flow rates during filtration experiments using HY10 membranes are provided in Fig. S16. Particle concentrations in membrane retentate measured using LIBD are presented in Fig. S17.

Increasing the concentration of PS particles in feed water resulted in greater deposition (Fig. 7A) at a constant permeate flux and drag force (Fig. 7B), which is consistent with previously reported particle deposition trends (Boussu et al., 2007). Overall, approximately 50–80% of the PS particles initially in the feed water were deposited by the end of the filtration experiments. Given the extent of deposition and assuming tightly packed particles with a fixed cross-sectional surface area, coverage of the membrane surface ranged from negligible at a concentration of 30 µg/L to an average of >4 monolayers at 500 µg/L. Increasing particle concentration and deposition resulted in greater release during backwash (Fig. 7C) at a constant backwash flux and drag force (Fig. 7D). Lower release efficiency at concentrations ≤200 µg/L (15–30% of deposited particles), where thinner particle deposits formed

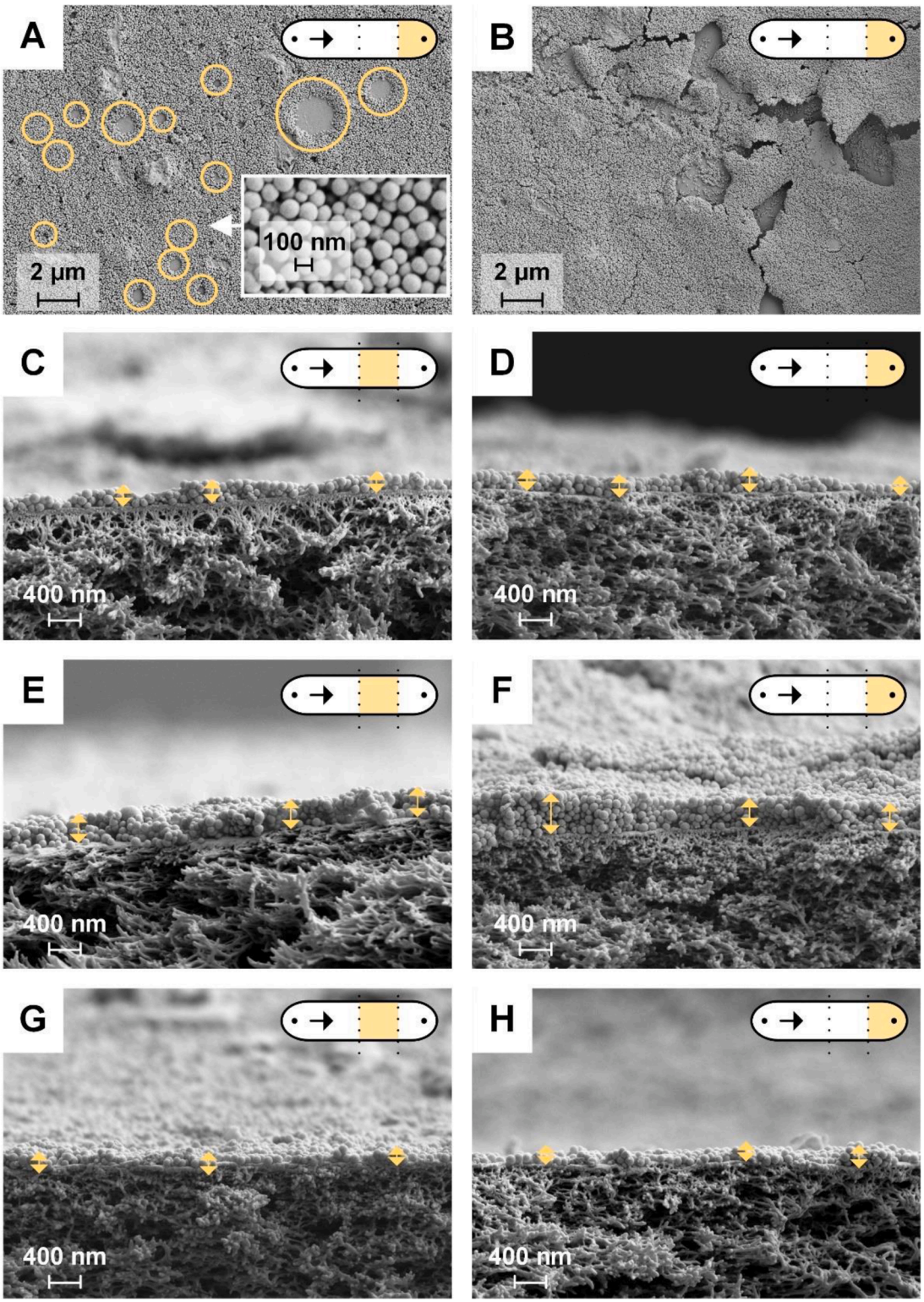

Fig. 8. (A and B) SEM images of the top surface of HY10 membranes after filtration with 100 μg/L and 500 μg/L of 100 nm PS particles, respectively (yellow circles indicate spots without PS particles). Cross-sections at the membrane surface (arrows indicate PS layer thickness) for HY10 membrane with 100 μg/L PS particles (C and D), HY10 membrane with 500 μg/L PS particles (E and F), and NF270 with 100 μg/L PS particles (G and H). Schematics in the top right corner of C–H indicate the location on membrane samples where the images were taken. Flux values during filtration experiments with HY10 and NF270 membranes were 500 and 200 L/m^2.h, respectively.

compared to 400–500 μg/L (40% of deposited particles), suggests that particle–membrane interactions were more difficult to overcome during backwash than particle–particle interactions (Lohaus et al., 2020).

Increasing the concentration of PS particles in feed water resulted in both greater particle deposition during permeation and release during backwash. Further investigation was undertaken to identify how particle release evolved with increasing deposition and cake layer thickness. To elucidate particle release mechanisms during backwash, SEM images of

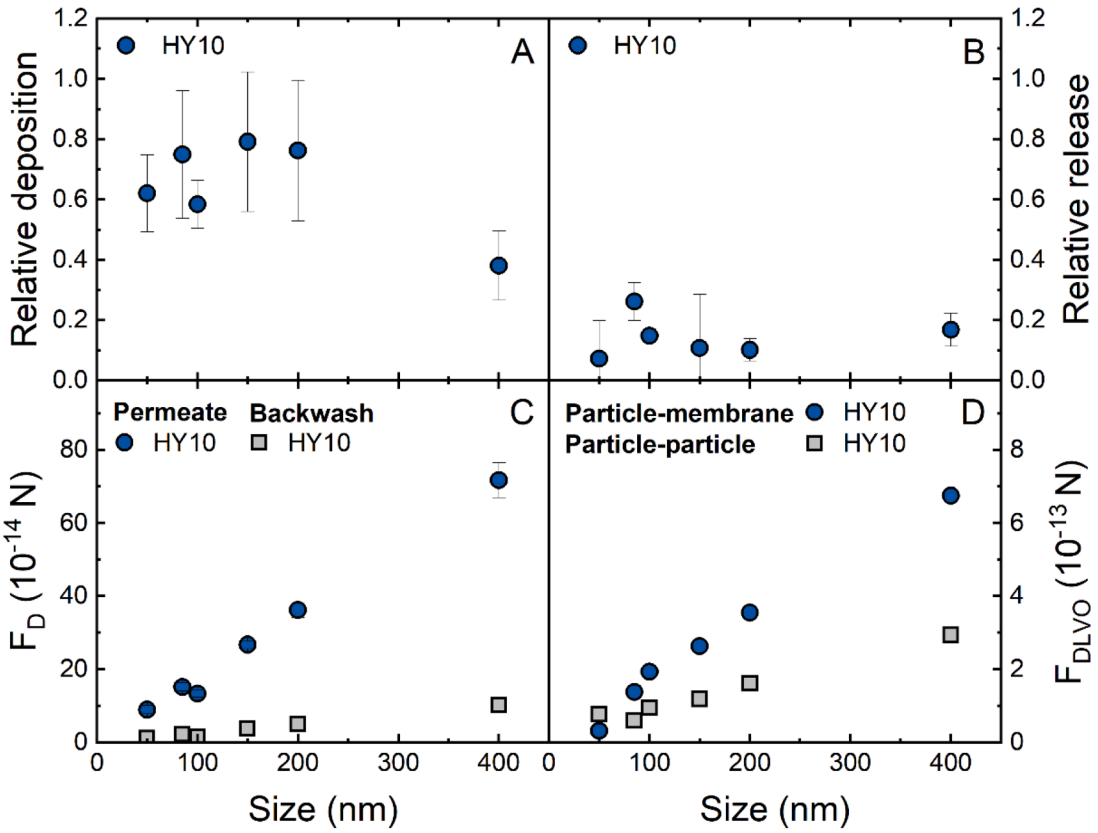

Fig. 9. Relative (A) deposition and (B) release of PS particles (20–400 nm), as well as (C) permeate/backwash drag forces and (D) maximum particle-membrane/particle-particle DLVO attractive forces. Feed water: $1.8{\cdot}10^8$ part./mL target concentration for PS particles (except 400 nm size which had a target concentration of $2.8{\cdot}10^6$ part./mL), 1 mM $NaHCO_3$, 10 mM NaCl; HY10 membrane; 500 L/m^2.h permeate flux, 54 L/m^2.h backwash flux.

HY10 and NF270 membrane samples were obtained following filtration experiments with low (100 μg/L) and high (500 μg/L) concentrations of PS particles (Fig. 8).

For HY10 membranes and feed water with 100 μg/L of PS particles, exposed circular spots were observed on the membrane surface where PS particles were not present (Fig. 8A), indicating that backwash flow concentrated at these locations resulted in particle release. For a thicker deposit observed with 500 μg/L of PS particles, backwash resulted in fracturing of the cake layer (Fig. 8B), demonstrating varied particle release mechanisms as a function of cake layer thickness. Similarly, an investigation of the dynamic behavior of cake layers during backwash revealed that thin deposits released as fragments that disaggregated in the bulk, whereas thick cake layers bent then fractured (Lüken et al., 2020). When considering membrane cross-sections, thin deposits (1−3 layers of PS particles) were observed for feed water with 100 μg/L of PS particles, which did not vary substantially in thickness between the third (Fig. 8C) and fourth quarters (Fig. 8D) of the membrane samples. At a particle concentration of 500 μg/L, greater cake layer thicknesses (4−5 layers of PS particles) were observed at select positions in the third (Fig. 8E) and fourth quarters (Fig. 8F), while thin deposits similar to those formed at 100 μg/L were observed for NF270 membranes (Fig. 8G andH). The SEM image shown in Fig. 8B only captures a small region having a thicker deposit; analyses of multiple SEM images reveal substantial differences in cake layer thickness between positions, although the higher concentration (500 μg/L) can be associated with an overall thicker cake layer (Fig. S18). This finding agreed with the LIBD results showing that particle deposition increased with feed water concentration (Fig. 7A).

To justify the different particle release mechanisms observed on membrane samples following backwash (*i.e.,* exposed circular spots and fractured cake layer), a force balance was performed using backwash drag and van der Waals forces for thin and thick deposit layers (Fig. S19).

3.5. *Variation of deposition and release with particle size*

To investigate the size dependence of particle deposition and release, filtration experiments were performed using 50–400 nm PS particles (Fig. 9). Anticipated particle trajectories are provided in Fig. S20, and particle–membrane as well as particle–particle interaction forces are presented in Fig. S21. Feed pressure, feed and permeate conductivity, feed flow rate, as well as permeate and backwash flow rates during filtration experiments using HY10 membranes are provided in Fig. S22. Particle concentrations in membrane retentate measured using LIBD are provided in Fig. S23.

Particle deposition did not vary substantially with particle size, ranging from approximately 60–100% for 50–200 nm PS particles and 30–60% for 400 nm PS particles (Fig. 9A), while release during backwash ranged from 10–30% for all particle sizes (Fig. 9B). Deposition occurs for all particle sizes as the applied permeate flux (500 L/m^2.h) exceeds the estimated critical flux values. The critical flux decreased from 47 to 11 L/m^2.h as particle size increased from 50–400 nm (Fig. S7), similar to experimental observation in a previous study (Kwon et al., 2000). Back-diffusion determined from the Stokes−Einstein equation decreases while permeate drag force increases with increasing particle size (Figs. 9C and S20), so in theory this should lead to stronger particle deposition for the larger particles. However, it is not the case as 400 nm particles deposited less than 50−200 nm particles. It can be implied that electrostatic repulsion, which increases with particle size, played a decisive role. The maximum particle−membrane and particle−particle DLVO attractive forces exhibited a linear increase with particle size (Fig. 9D), which was accompanied by increases in the

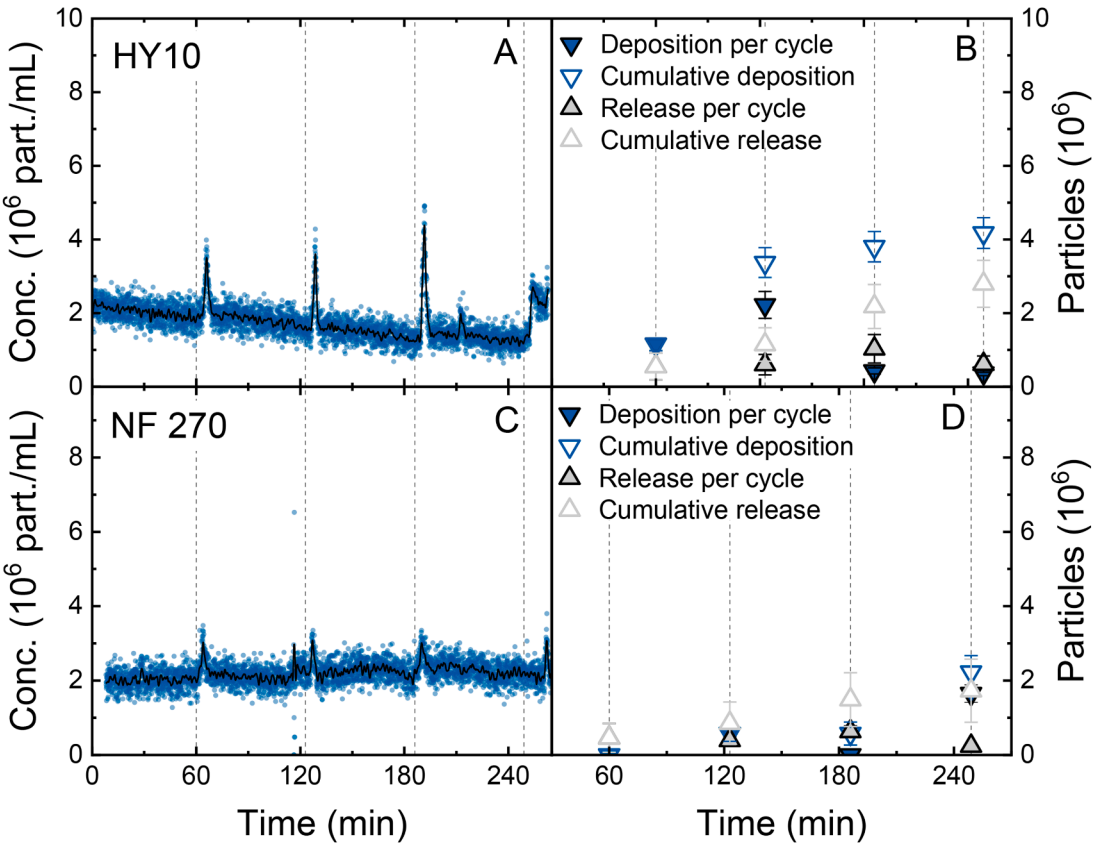

Fig. 10. (A) Retentate concentration and (B) deposition and release of weathered NPs over four cycles for HY10 membranes, as well as (C) retentate concentration and (D) deposition and release of weathered NPs over four cycles for NF270 membranes. Feed water: 1 μg/L weathered NPs (approximately $1.8{\cdot}10^6$ part./mL), 1 mM $NaHCO_3$, 10 mM NaCl; 500 L/m^2.h (HY10) and 200 L/m^2.h (NF270) permeate flux, 54 L/m^2.h backwash flux.

repulsive energy barrier, suggesting weaker adhesion in the secondary minimum (Fig. S21).

It was demonstrated that LIBD is suitable for investigating the deposition and release of model nanoparticles at low concentrations. However, additional evaluation is required to determine if LIBD can be applied to quantify the transport behavior of environmentally relevant NPs, which exhibit heterogeneity in shape, size, and surface area. Despite these morphological complexities, LIBD has been shown to exhibit higher sensitivity towards weathered NPs in previous work (Nguyen et al., 2025).

3.6. Deposition and release of weathered nanoplastics

To determine if LIBD is suitable for quantifying the deposition and release of environmentally relevant NPs, filtration experiments were performed using weathered NPs with both HY10 and NF270 membranes (Fig. 10). Due to the high sensitivity of LIBD towards weathered NPs, the initial concentration was set three orders of magnitude lower than that for PS particles. Feed pressure, feed and permeate conductivity, feed flow rate, as well as permeate and backwash flow rates during filtration experiments using HY10 and NF270 membranes are provided in Fig. S24.

A decline in the concentration of weathered NPs in membrane retentate and clear concentration spikes exceeding the LOD for LIBD were observed following backwash for each cycle (Fig. 10A), suggesting that LIBD can be used to quantify the deposition and release of weathered NPs during NF. For HY10 membranes, 12% of weathered NPs ($2.2 \pm 0.3{\cdot}10^5$ particles) initially present in feed water deposited at the first instances of the first cycle and approximately 43% after four cycles (Fig. 10B). The release efficiency of deposited NPs during backwash was approximately 35%, similar to that observed for PS particles. Despite a four-orders-of-magnitude difference in the initial particle concentration, similar particle deposition (19–40%) and release (15–21%) were reported for polyethylene fragments (93±1 nm average size) during ultrafiltration (Enfrin et al., 2021). Results from the present study indicate that even at environmentally relevant concentrations, NPs can irreversibly accumulate on membrane surfaces, raising questions about the implications for long-term membrane performance. For NF270, NP concentration remained relatively constant over the course of filtration, while some small peaks that indicate backwash were observed (Fig. 10C). This means the cumulative release of NPs are negligible and within the range of error bars (Fig. 10D). It is possible that due to low deposition and high release, the surface of the membrane was not fully covered by weathered NPs as observed using SEM (Fig. S25). These results suggest that weathered NPs exhibit reduced interfacial interactions compared to PS particles. Reduced interfacial interactions could be due to increased hydrophilicity and hydration repulsion of weathered NPs resulting from the formation of carbonyl and polar functional groups during the weathering process (Tao et al., 2022, Xu et al., 2021). Further investigation is required to gain a detailed understanding of how heterogeneous particle properties alter deposition and release behavior during NF.

4. Conclusions

The objective of this research was to evaluate LIBD as an analytical tool for quantifying the deposition and release of NPs in real-time during NF, and to gain insight regarding the fate of NPs under different NF operating conditions and particle properties. The sensitivity of LIBD was showcased by successfully quantifying 50–400 nm sized PS particles as well as weathered NPs at environmentally relevant concentrations (1–500 μg/L). This enables the implementation of LIBD in real water

treatment plants (although the handling of interferants from water still requires further investigation), alongside research on fundamental particle−membrane interactions.

At permeate fluxes beyond 50−100 L/m^2.h, critical flux was exceeded and the cumulative deposition of PS particles following four cycles was sufficient to completely cover the surface of both HY10 and NF270 membranes. Particle deposition measured using LIBD was consistent with that anticipated based on particle trajectories that were estimated from tangential and permeate drag forces. Calculation of DLVO forces indicated that weak particle adhesion occurred in a secondary minimum less than half a particle diameter from the membrane/cake layer surface, as the presence of a repulsive force barrier prevented particle–membrane and particle–particle adhesion at shorter separation distances. These analyses provided theoretical justification for the observations made using LIBD. Only a limited portion ($\leq$ 40%) of deposited PS particles were released during backwash despite increasing backwash flux, indicating that backwash drag forces attainable in the present study were insufficient to fully overcome particle–membrane and particle–particle interactions. The extensive coverage of membranes by NPs, even at low environmentally relevant concentrations, combined with poor release efficiency during backwashing, may alter membrane surface properties and fouling behavior, having important operational implications that warrant further consideration.

Increasing the concentration of PS particles in feed water resulted in greater particle deposition and release during backwash. Visualization of membrane samples using SEM revealed that the release of deposited particles during backwash proceeded via two distinct mechanisms: i) complete release from small circular spots near membrane pores for thin deposits (1–3 layers of PS particles), and ii) partial release and fractured cake layers for thick deposits (4–5 layers of PS particles). This demonstrates the potential application of LIBD and SEM to support research regarding particle release mechanisms during backwash and the development of new strategies to enhance cleaning efficiency for NPs. Neither particle deposition nor release varied substantially with particle size (50–400 nm), as the applied permeate flux exceeded the estimated critical flux. For weathered NPs, lower deposition and higher release efficiency were observed when compared to PS particles. The heterogeneous properties of weathered NPs likely altered their transport behavior as well as interfacial interactions at the membrane surface, requiring further investigation for a more complete understanding. The ability to quantitatively study the deposition and release of weathered NPs using LIBD is particularly promising as heterogeneous particle-membrane interactions remain poorly understood despite their practical relevance.

CRediT authorship contribution statement

Tyler A. Malkoske: Conceptualization, Formal analysis, Investigation, Methodology, Writing – original draft. **Minh N. Nguyen:** Conceptualization, Formal analysis, Investigation, Methodology, Writing – review & editing. **Susanne Erpel:** Investigation, Methodology. **Marcus Wyss:** Investigation, Resources. **Andrea I. Schäfer:** Conceptualization, Funding acquisition, Methodology, Project administration, Resources, Supervision, Writing – review & editing.

Declaration of competing interest

The authors declare that they have no known competing financial interests or personal relationships that could have appeared to influence the work reported in this paper.

Acknowledgements

The authors thank the Helmholtz Recruitment Initiative for KIT-IAMT lab and project funding. Nitto Hydranautics and DuPont are appreciated for providing the HY10 and NF270 membranes, respectively. Malvern Panalytical is appreciated for providing a demo NTA system for the examination of aggregation. Ines Zucker, Andrey E. Rubin and Noa Sand (TAU, Israel) are thanked for the preparation of environmentally relevant nanoplastics used in this work. We appreciate Pia Lipp (DVGW-TZW) for providing the Excel macro for LIBD data analysis and providing insight into the coupling of LIBD with membrane filtration systems. Muriel Bouby (INE, KIT) is thanked for critical discussions regarding LIBD operation. Akhil Gopalakrishnan and Yang-Hui Cai (IAMT, KIT) are acknowledged for discussions about membrane−particle interactions and filtration−backwash system operation. Gabriel Glossner (IAMT, KIT) is appreciated for assisting with method development, performing LIBD experiments, and contributing to preliminary data analysis.

Supplementary materials

Supplementary material associated with this article can be found, in the online version, at doi:10.1016/j.watres.2026.126362.

Data availability

Data will be made available on request.

References

Al-Amoudi, A., Lovitt, R.W., 2007. Fouling strategies and the cleaning system of NF membranes and factors affecting cleaning efficiency. J. Membr. Sci. 303 (1), 4–28.
Ali, N., Katsouli, J., Marczylo, E.L., Gant, T.W., Wright, S., Bernardino de la Serna, J., 2024. The potential impacts of micro-and-nano plastics on various organ systems in humans. EBioMedicine 99, 104901.
Altmann, J., Ripperger, S., 1997. Particle deposition and layer formation at the crossflow microfiltration. J. Membr. Sci. 124 (1), 119–128.
Austin, J., Minelli, C., Hamilton, D., Wywijas, M., Jones, H.J., 2020. Nanoparticle number concentration measurements by multi-angle dynamic light scattering. J. Nanoparticle Res. 22 (5), 108.
Bacchin, P., Aimar, P., Field, R.W., 2006. Critical and sustainable fluxes: theory, experiments and applications. J. Membr. Sci. 281 (1), 42–69.
Bacchin, P., Aimar, P., Sanchez, V., 1995. Model for colloidal fouling of membranes. AIChE J. 41 (2), 368–376.
Belfort, G., Davis, R.H., Zydney, A.L., 1994. The behavior of suspensions and macromolecular solutions in crossflow microfiltration. J. Membr. Sci. 96 (1), 1–58.
Besseling, E., Wang, B., Lürling, M., Koelmans, A.A., 2014. Nanoplastic affects growth of S. obliquus and reproduction of D. magna. Environ. Sci. Technol. 48 (20), 12336–12343.
Birch, Q.T., Potter, P.M., Pinto, P.X., Dionysiou, D.D., Al-Abed, S.R., 2020. Sources, transport, measurement and impact of nano and microplastics in urban watersheds. Rev. Environ. Sci. Biotechnol. 19 (2), 275–336.
Blancho, F., Davranche, M., Fumagalli, F., Ceccone, G., Gigault, J., 2021. A reliable procedure to obtain environmentally relevant nanoplastic proxies. Environ. Sci. Nano 8 (11), 3211–3219.
Boucher, J., Faure, F., Pompini, O., Plummer, Z., Wieser, O., Felippe de Alencastro, L., 2019. Micro) plastic fluxes and stocks in Lake Geneva basin. TrAC Trends Anal. Chem. 112, 66–74.
Boussu, K., Belpaire, A., Volodin, A., Van Haesendonck, C., Van der Meeren, P., Vandecasteele, C., Van der Bruggen, B., 2007. Influence of membrane and colloid characteristics on fouling of nanofiltration membranes. J. Membr. Sci. 289 (1), 220–230.
Boussu, K., De Baerdemaeker, J., Dauwe, C., Weber, M., Lynn, K.G., Depla, D., Aldea, S., Vankelecom, I.F.J., Vandecasteele, C., Van der Bruggen, B., 2007. Physico-chemical characterization of nanofiltration membranes. ChemPhysChem 8 (3), 370–379.
Bowen, W.R., Mohammad, A.W., 1998. Characterization and prediction of nanofiltration membrane performance - A general assessment. Chem. Eng. Res. Des. 76 (8), 885–893.
Brant, J.A., Childress, A.E., 2002. Assessing short-range membrane–colloid interactions using surface energetics. J. Membr. Sci. 203 (1), 257–273.
Cai, Y.H., Boussouga, Y.A., Schäfer, A.I., 2024. Renewable energy powered membrane technology: impact of intermittency on membrane integrity. Desalination 580, 117504.
Cai, Y.H., Burkhardt, C.J., Schäfer, A.I., 2021. Renewable energy powered membrane technology: impact of osmotic backwash on scaling during solar irradiance fluctuation. J. Membr. Sci. 619, 118799.
Cai, Y.H., Gopalakrishnan, A., Deshmukh, K.P., Schäfer, A.I., 2022. Renewable energy powered membrane technology: implications of adhesive interaction between membrane and organic matter on spontaneous osmotic backwash cleaning. Water Res. 221, 118752.
2018. California Code of Regulations. California safe drinking water act, health and safety code 116376.

Cleveland, W.S., 1979. Robust locally weighted regression and smoothing scatterplots. J. Am. Stat. Assoc. 74 (368), 829–836.
Cohen, R.D., Probstein, R.F., 1986. Colloidal fouling of reverse osmosis membranes. J. Colloid Interface Sci. 114 (1), 194–207.
Derjaguin, B., Landau, L., 1941. Theory of the stability of strongly charged lyophobic sols and of the adhesion of strongly charged particles in solutions of electrolytes. Acta Physicochim. URSS 14, 733.
Ekvall, M.T., Stábile, F., Hansson, L.A., 2024. Nanoplastics rewire freshwater food webs. Commun. Earth Environ. 5 (1), 486.
El Hadri, H., Gigault, J., Maxit, B., Grassl, B., Reynaud, S., 2020. Nanoplastic from mechanically degraded primary and secondary microplastics for environmental assessments. NanoImpact 17, 100206.
Enfrin, M., Lee, J., Fane, A.G., Dumee, L.F., 2021. Mitigation of membrane particulate fouling by nano/microplastics via physical cleaning strategies. Sci. Total Environ. 788, 147689.
Fane, A.G., Tang, C.Y., Wang, R., 2011. 4.11 - membrane technology for water: microfiltration, ultrafiltration, nanofiltration, and reverse osmosis. Wilderer, P. (Ed.). Treatise on Water Science. Elsevier, Oxford, pp. 301–335.
Farhat, N.M., Christodoulou, C., Placotas, P., Blankert, B., Sallangos, O., Vrouwenvelder, J.S., 2020. Cartridge filter selection and replacement: optimization of produced water quantity, quality, and cost. Desalination 473, 114172.
Feng, X., Manek, V., Andrews, R.C., Almuhtaram, H., 2025. Sub-sampling strategies for analysis of small (<20 μm) microplastics in water. Water Res. 283, 123846.
Field, R.W., Wu, D., Howell, J.A., Gupta, B.B., 1995. Critical flux concept for microfiltration fouling. J. Membr. Sci. 100 (3), 259–272.
Filipe, V., Hawe, A., Jiskoot, W., 2010. Critical evaluation of nanoparticle tracking analysis (NTA) by NanoSight for the measurement of nanoparticles and protein aggregates. Pharm. Res. 27 (5), 796–810.
Gigault, J., El Hadri, H., Nguyen, B., Grassl, B., Rowenczyk, L., Tufenkji, N., Feng, S., Wiesner, M., 2021. Nanoplastics are neither microplastics nor engineered nanoparticles. Nat. Nanotechnol. 16 (5), 501–507.
Gigault, J., Halle, A.t., Baudrimont, M., Pascal, P.Y., Gauffre, F., Phi, T.L., El Hadri, H., Grassl, B., Reynaud, S., 2018. Current opinion: what is a nanoplastic? Environ. Pollut. 235, 1030–1034.
Gross, J., Sayle, S., Karow, A.R., Bakowsky, U., Garidel, P., 2016. Nanoparticle tracking analysis of particle size and concentration detection in suspensions of polymer and protein samples: influence of experimental and data evaluation parameters. Eur. J. Pharm. Biopharm. 104, 30–41.
Hartmann, N.B., Hüffer, T., Thompson, R.C., Hassellöv, M., Verschoor, A., Daugaard, A. E., Rist, S., Karlsson, T., Brennholt, N., Cole, M., Herrling, M.P., Hess, M.C., Ivleva, N. P., Lusher, A.L., Wagner, M., 2019. Are we speaking the same language? Recommendations for a definition and categorization framework for plastic debris. Environ. Sci. Technol. 53 (3), 1039–1047.
He, P., Chen, L., Shao, L., Zhang, H., Lü, F., 2019. Municipal solid waste (MSW) landfill: a source of microplastics? -Evidence of microplastics in landfill leachate. Water Res. 159, 38–45.
Hong, S., Faibish, R.S., Elimelech, M., 1997. Kinetics of permeate flux decline in crossflow membrane filtration of colloidal suspensions. J. Colloid Interface Sci. 196 (2), 267–277.
Huang, X., Bhattacharjee, S., Hoek, E.M.V., 2010. Is surface roughness a "scapegoat" or a primary factor when defining particle−substrate interactions? Langmuir 26 (4), 2528–2537.
Hwang, K.J., Mei-Chou, Y., Lu, W.M., 1997. Migration and deposition of submicron particles in crossflow microfiltration. Sep. Sci. Technol. 32 (17), 2723–2747.
Imbrogno, A., Calvo, J.I., Breida, M., Schwaiger, R., Schäfer, A.I., 2025. Molecular weight cut off (MWCO) determination in ultra- and nanofiltration: review of methods and implications on organic matter removal. Sep. Purif. Technol. 354, 128612.
Israelachvili, J.N., 1978. Measurement of forces between surfaces immersed in electrolyte solutions. Faraday Discuss. Chem. Soc. 65 (0), 20–24.
Jambeck, J.R., Geyer, R., Wilcox, C., Siegler, T.R., Perryman, M., Andrady, A., Narayan, R., Law, K.L., 2015. Plastic waste inputs from land into the ocean. Science 347 (6223), 768–771.
Kalde, A.M., Lohaus, J., Musholt, S., Wessling, M., 2023. On the balance of hydrophilicity and electrostatic interactions during particle filtration and backwash at microfiltration pores. J. Membr. Sci. 680, 121640.
Kernchen, S., Löder, M.G.J., Fischer, F., Fischer, D., Moses, S.R., Georgi, C., Nölscher, A. C., Held, A., Laforsch, C., 2022. Airborne microplastic concentrations and deposition across the Weser river catchment. Sci. Total Environ. 818, 151812.
Kim, S., Marion, M., Jeong, B.H., Hoek, E.M.V., 2006. Crossflow membrane filtration of interacting nanoparticle suspensions. J. Membr. Sci. 284 (1), 361–372.
Kuznetsova, L.A., Bazou, D., Coakley, W.T., 2007. Stability of 2-D colloidal particle aggregates held against flow stress in an ultrasound trap. Langmuir 23 (6), 3009–3016.
Kwon, D.Y., Vigneswaran, S., Fane, A.G., Aim, R.B., 2000. Experimental determination of critical flux in cross-flow microfiltration. Sep. Purif. Technol. 19 (3), 169–181.
Lebreton, L., Andrady, A., 2019. Future scenarios of global plastic waste generation and disposal. Palgrave Commun. 5 (1), 6.
Lee, H., Im, S.J., Lee, H., Kim, C.M., Jang, A., 2021. Comparative analysis of salt cleaning and osmotic backwash on calcium-bridged organic fouling in nanofiltration process. Desalination 507, 115022.
Lee, T., Charrault, E., Neto, C., 2014. Interfacial slip on rough, patterned and soft surfaces: a review of experiments and simulations. Adv. Colloid Interface Sci. 210, 21–38.
Lee, S., Lee, C.H., 2006. Microfiltration and ultrafiltration as a pretreatment for nanofiltration of surface water. Sep. Sci. Technol. 41 (1), 1–23.
Li, Z., Yan, L., Junaid, M., Chen, X., Liao, H., Gao, D., Wang, Q., Zhang, Y., Wang, J., 2023. Impacts of polystyrene nanoplastics at the environmentally relevant and sub-lethal concentrations on the oxidative stress, immune responses, and gut microbiota to grass carp (Ctenopharyngodon idella). J. Hazard. Mater. 441, 129995.
Liu, J., Huang, T., Ji, R., Wang, Z., Tang, C.Y., Leckie, J.O., 2020. Stochastic collision–attachment-based Monte Carlo simulation of colloidal fouling: transition from foulant–clean-membrane interaction to foulant–fouled-membrane interaction. Environ. Sci. Technol. 54 (19), 12703–12712.
Liu, J., Wang, Z., Tang, C.Y., Leckie, J.O., 2018. Modeling dynamics of colloidal fouling of RO/NF membranes with a novel collision-attachment approach. Environ. Sci. Technol. 52 (3), 1471–1478.
Liu, W., Liao, H., Wei, M., Junaid, M., Chen, G., Wang, J., 2024. Biological uptake, distribution and toxicity of micro(nano)plastics in the aquatic biota: a special emphasis on size-dependent impacts. TrAC Trends Anal. Chem. 170, 117477.
Liu, X., Yang, Y., Graham, N.J.D., Takizawa, S., Ng, H.Y., 2025. Deciphering membrane biofouling induced by micro-/nano-plastics in nanofiltration: Metagenomic insights and spacer-driven mitigations. Water Res. 281, 123682.
Liu, X., Yang, Y., Takizawa, S., Graham, N.J.D., Chen, C., Pu, J., Ng, H.Y., 2024. New insights into the concentration-dependent regulation of membrane biofouling formation via continuous nanoplastics stimulation. Water Res. 253, 121268.
Lüken, A., Linkhorst, J., Fröhlingsdorf, R., Lippert, L., Rommel, D., De Laporte, L., Wessling, M., 2020. Unravelling colloid filter cake motions in membrane cleaning procedures. Sci. Rep. 10 (1), 20043.
Lohaus, J., Stockmeier, F., Surray, P., Lölsberg, J., Wessling, M., 2020. What are the microscopic events during membrane backwashing? J. Membr. Sci. 602, 117886.
Malkoske, T.A., Bérubé, P.R., Andrews, R.C., 2025. Hydraulic and chemical cleaning efficiency for the release of microplastics retained during coagulation/flocculation-ultrafiltration. Water Res. 282, 123601.
Mason, S.A., Garneau, D., Sutton, R., Chu, Y., Ehmann, K., Barnes, J., Fink, P., Papazissimos, D., Rogers, D.L., 2016. Microplastic pollution is widely detected in US municipal wastewater treatment plant effluent. Environ. Pollut. 218, 1045–1054.
Materić, D., Peacock, M., Dean, J., Futter, M., Maximov, T., Moldan, F., Röckmann, T., Holzinger, R., 2022. Presence of nanoplastics in rural and remote surface waters. Environ. Res. Lett. 17 (5), 054036.
Mänttäri, M., Nyström, M., 2000. Critical flux in NF of high molar mass polysaccharides and effluents from the paper industry. J. Membr. Sci. 170 (2), 257–273.
Nguyen, M.N., Lipp, P., Zucker, I., Schäfer, A.I., 2025. Quantification of nanoplastics and inorganic nanoparticles via laser-induced breakdown detection (LIBD). Small Methods (2402060), 1–14.
OECD, Global Plastics Outlook: Policy Scenarios to 2060. https://www.oecd.org/content/dam/oecd/en/publications/reports/2022/06/global-plastics-outlook_f065ef59/aa1edf33-en.pdf (2026).
Richards, B.S., Capão, D.P.S., Früh, W.G., Schäfer, A.I., 2015. Renewable energy powered membrane technology: Impact of solar irradiance fluctuations on performance of a brackish water reverse osmosis system. Sep. Purif. Technol. 156, 379–390.
Rossé, P., Loizeau, J.L., 2003. Use of single particle counters for the determination of the number and size distribution of colloids in natural surface waters. Colloids Surf. A Physicochem. Eng. Asp. 217 (1), 109–120.
Santos, F.A., Andre, R.S., Alvarenga, A.D., Alves, A.L.M.M., Correa, D.S., 2025. Micro- and nanoplastics in the environment: a comprehensive review on detection techniques. Environ. Sci. Nano 12 (7), 3442–3467.
Sarkar, A.K., Rubin, A.E., Zucker, I., 2021. Engineered polystyrene-based microplastics of high environmental relevance. Environ. Sci. Technol. 55 (15), 10491–10501.
Scherbaum, F.J., Knopp, R., Kim, J.I., 1996. Counting of particles in aqueous solutions by laser-induced photoacoustic breakdown detection. Appl. Phys. B 63 (3), 299–306.
Shi, C., Liu, Z., Yu, B., Zhang, Y., Yang, H., Han, Y., Wang, B., Liu, Z., Zhang, H., 2024. Emergence of nanoplastics in the aquatic environment and possible impacts on aquatic organisms. Sci. Total Environ. 906, 167404.
Song, L., Elimelech, M., 1995. Particle deposition onto a permeable surface in laminar flow. J. Colloid Interface Sci. 173 (1), 165–180.
Syberg, K., Nielsen, M.B., Westergaard Clausen, L.P., van Calster, G., van Wezel, A., Rochman, C., Koelmans, A.A., Cronin, R., Pahl, S., Hansen, S.F., 2021. Regulation of plastic from a circular economy perspective. Curr. Opin. Green Sustain. Chem. 29, 100462.
Tang, C.Y., Chong, T.H., Fane, A.G., 2011. Colloidal interactions and fouling of NF and RO membranes: a review. Adv. Colloid Interface Sci. 164 (1), 126–143.
Tao, H., Yang, L., Qi, Y., Chen, Y., Yu, D., Zhou, L., Lin, T., Xu, H., Song, J., 2022. Deposition of polystyrene microplastics on bare or biofilm-coated silica analysed via QCM-D. Sci. Total Environ. 847, 157661.
ten Hietbrink, S., Materić, D., Holzinger, R., Groeskamp, S., Niemann, H., 2025. Nanoplastic concentrations across the North Atlantic. Nature 643 (8071), 412–416.
Van der Bruggen, B., Segers, D., Vandecasteele, C., Braeken, L., Volodin, A., Van Haesendonck, C., 2005. How a microfiltration pretreatment affects the performance in nanofiltration. Sep. Sci. Technol. 39 (7), 1443–1459.
Verwey, E.J.W., 1947. Theory of the stability of lyophobic colloids. J. Phys. Colloid Chem. 51 (3), 631–636.
Vrijenhoek, E.M., Hong, S., Elimelech, M., 2001. Influence of membrane surface properties on initial rate of colloidal fouling of reverse osmosis and nanofiltration membranes. J. Membr. Sci. 188 (1), 115–128.
Walther, C., Cho, H.R., Fanghänel, T., 2004. Measuring multimodal size distributions of aquatic colloids at trace concentrations. Appl. Phys. Lett. 85 (26), 6329–6331.
Winiarska, E., Jutel, M., Zemelka-Wiacek, M., 2024. The potential impact of nano- and microplastics on human health: Understanding human health risks. Environ. Res. 251, 118535.

Xu, Y., Ou, Q., He, Q., Wu, Z., Ma, J., Huangfu, X., 2021. Influence of dissolved black carbon on the aggregation and deposition of polystyrene nanoplastics: comparison with dissolved humic acid. Water Res. 196, 117054.
Xu, Y., Ou, Q., Jiao, M., Liu, G., van der Hoek, J.P., 2022. Identification and quantification of nanoplastics in surface water and groundwater by pyrolysis gas chromatography-mass spectrometry. Environ. Sci. Technol. 56 (8), 4988–4997.
Xu, Y., Ou, Q., Wang, X., van der Hoek, J.P., Liu, G., 2024. Mass concentration and removal characteristics of microplastics and nanoplastics in a drinking water treatment plant. ACS ES&T Water 4 (8), 3348–3358.
Yang, Q., Zhang, J., Zhang, N., Wang, D., Yuan, X., Tang, C.Y., Gao, B., Wang, Z., 2024. Impact of nanoplastics on membrane scaling and fouling in reverse osmosis desalination process. Water Res. 249, 120945.
Zhang, J., Ding, W., Zou, G., Wang, X., Zhao, M., Guo, S., Chen, Y., 2023. Urban pipeline rainwater runoff is an important pathway for land-based microplastics transport to inland surface water: a case study in Beijing. Sci. Total Environ. 861, 160619.
Zhou, Y., Wu, C., Li, Y., Jiang, H., Miao, A., Liao, Y., Pan, K., 2023. Effects of nanoplastics on clam Ruditapes philippinarum at environmentally realistic concentrations: Toxicokinetics, toxicity, and gut microbiota. J. Hazard. Mater. 456, 131647.
Zhu, X., Hoffman, M.J., Rochman, C.M., 2024. A city-wide emissions inventory of plastic pollution. Environ. Sci. Technol. 58 (7), 3375–3385.
Zuri, G., Karanasiou, A., Lacorte, S., 2023. Microplastics: Human exposure assessment through air, water, and food. Environ. Int. 179, 108150.